The role of gravity in the asymmetry of flames in narrow combustion chambers

Kevin Bioche, Amanda Pieyre, Guillaume Ribert, Franck Richecoeur, Luc Vervisch

The role of gravity in the asymmetry of flames in narrow combustion chambers

Kevin Bioche[a], Amanda Pieyre[b], Guillaume Ribert[a,*], Franck Richecoeur[b], Luc Vervisch[a]

[a]*CORIA - CNRS, Normandie Université, INSA de Rouen, Technopole du Madrillet, BP 8 76801 Saint-Etienne-du-Rouvray, France*
[b]*EM2C - CNRS, CentraleSupélec, Université Paris-Saclay, 3 rue Joliot Curie 91192 Gif Sur Yvette cedex, France*

Abstract

The symmetry breaking of a lean premixed laminar methane/air flame, propagating in an horizontal narrow tube of internal diameter $\ell_i = 5$ mm, is investigated experimentally and numerically. The methane/air flame numerical simulations performed include complex molecular transport and the fully coupled solving of heat transfer at and within the wall. In place of a symmetrical flame, experiments show the stability of a slanted flame with a preferential anchoring at the top. This is observed for both flames freely propagating along isothermal (T = 300 K) walls, and flames stabilized by the incoming flow and thermally coupled with heat transfer inside the walls. Numerical simulations with and without gravity demonstrate its preponderant contribution in the symmetry breaking. The slight flow stratification is sufficient to break the symmetry, with a dominant role of the baroclinic torque, leading to a specific deviation of the incoming streamlines observed both experimentally and numerically.

Keywords: Narrow channel, Flame symmetry, Experiments, Numerical simulation, Gravity effect, Flame wall interaction

*Corresponding author
Email address: ribert@coria.fr (Guillaume Ribert)

1. Introduction

In small-scale combustion, a vast amount of studies consider the problem as symmetric, either with respect to the middle plane in a flat channel or to the centerline in a tube [1–12]. However, recent numerical [13–16] and experimental [17, 18] studies reveal the apparition of non-symmetric flame shapes for various conditions. Depending on the configuration, the physical phenomena susceptible to break the symmetry are numerous and the objective of this work is to focus on the role of gravity.

Aside from gravity, at least three generic types of instabilities have been discussed in the literature, which could potentially promote a non-symmetrical laminar flame behaviour, namely Darrieus-Landau [19, 20], viscosity-induced Saffman-Taylor [21] and diffusive-thermal [22, 23] instabilities. The Darrieus-Landau instability is an amplification of the flame surface by hydrodynamic disturbances coming from gas expansion [24]. It was introduced to explain the predominance of slanted against symmetrical tulip-shaped flames, for a tube diameter exceeding a hundred times the flame thickness δ_F [13]. However, because this instability requires a minimal characteristic length to develop, such an asymmetry was not observed for lower diameters as those considered in this study (about $15\delta_F$). On another hand, the viscosity-induced Saffman-Taylor (S-T) instabilities [21, 25] are typical of combustion in narrow channels, as a result of viscous-induced pressure gradients, which are favoured by small channel dimensions [26]. In the development of the diffusive-thermal instabilities [22, 23], the Lewis number (Le) was found as a key parameter. For Le $<$ 1, the existence of non-symmetric flames is discussed in various studies [14–17, 27, 28]. Besides, in the context of a thermo-diffusive model, Le $>$ 1 flames with very low mass flow rate are also found asymmetric [15] and vibratory instability of the planar flame in the tube can develop [29]. Unity Lewis flames have been found symmetric when approaching the micro-combustion scale [9] and a stability analysis including heat loss also reports that unity Lewis number symmetric flames are stable [30]. All of these studies do not include the gravity in the analysis.

In small-scale combustion, gravity is often neglected because the Froude number (Fr), inversely

proportional to the characteristic length of the system, is expected larger than unity. For instance for methane burning in air under a fuel lean condition,

$$\mathrm{Fr} = \frac{S_\mathrm{L}^{\mathrm{o}\,2}}{g \times \ell_i} = 1.59\,, \tag{1}$$

where $g = 9.81\ \mathrm{m \cdot s^{-2}}$ denotes the acceleration of gravity, $S_\mathrm{L}^\mathrm{o} = 28\ \mathrm{cm \cdot s^{-1}}$ is the methane/air adiabatic flame speed at equivalence ratio 0.8 considered in this study [31] and $\ell_i = 5$ mm is the characteristic length of the tube diameter or channel width. Nonetheless, having $S_\mathrm{L}^{\mathrm{o}\,2} > g \times \ell_i$ indicates that gravitational effects do not fully drive the flame dynamics, but not necessarily that they can be completely neglected.

Experiments of flame propagation in horizontal tubes show the appearance of slanted flames with a preferential direction [17, 18]. So far this observation was explained by a flame stabilisation mechanism influenced by the free convection in the air surrounding the tube. A decrease of the Nusselt number toward the top of the cylinder, as the outside boundary layer thickens, has been reported in thermal and flow plume developing around heated tubes [32–34]. The plume insulates the cylinder from the surrounding air and the reaction zone in the upper part of the tube is then submitted to a lower heat transfer coefficient. Then gravity is driving the flame shape indirectly by affecting the flow surrounding the tube. A direct influence of gravity inside wide tubes was also discussed in the literature using a model equation for flame propagation [35], with buoyant induced effects affecting the flame shape inside the tube.

The objective of this paper is to progress on the understanding of these 'internal' gravity effects occurring inside the narrow combustion chamber by combining experiments and numerical simulations. The experimental and numerical set-up are first described. Then, the overall flames properties are reported, flames which are asymmetrical in all the conducted experiments. Two cases are studied, a flame freely propagating above an iso-thermal cold wall and a flame fixed in the laboratory frame, *i.e.* stabilised by the incoming flow, the latter subjected to strong coupling with wall heat transfer. The experimentally observed flame shape is reproduced by the simulation only in the presence of gravity and the breaking of symmetry is explained by the change of

behaviour of the baroclinic torque across the flame front after introducing gravity.

2. Experimental and numerical set-up

2.1. Experimental configuration

The experimental set-up shown in Fig. 1 consists in a $\ell_i = 5$ mm inner diameter and $e_w = 1$ mm thick quartz tube placed in horizontal position. The methane/air fresh mixture at a temperature $T_o = 300$ K flows from the left to the right at an equivalence ratio of 0.8, with a Reynolds number of about 50. The length of the tube is 200 mm. The mixture is first ignited at the free end of the tube $x_e = 150$ mm, then the mass flow rate is decreased for the flame to enter the tube, which may be stabilised at a given position for a bulk velocity of the incoming flow balancing its burning velocity.

The quartz was chosen for its thermal and optical properties, allowing for a direct visualization of the flame and its propagation. The diameter was fixed right above the quenching diameter of the mixture, according to the analysis reported in [36].

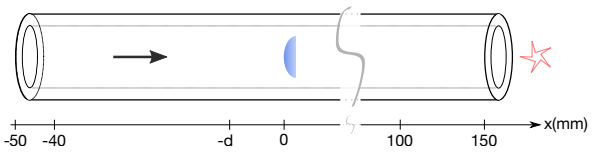

Figure 1: Schematic view of the experimental set-up composed of a quartz tube of $\ell_i = 5$ mm inner diameter and $e_w = 1$ mm thickness, inside which a lean methane/air mixture is injected. The inlet ($x_i = -50$ mm) is connected to the mass flow controllers while the outlet ($x_e = 150$ mm) is in open-air, where the flame is first ignited to then propagate inside the tube.

Two mass flow controllers (EL-FLOW Bronkhorst) with 0-700 Nml/min range for air and 0-70 Nml/min for methane are enslaved to command the velocity and equivalence ratio of the flow. A mixture chamber prior to the quartz tube entrance (not shown in Fig. 1) secures the premixing of the gas. With a precision of 0.35 mL/min, the mass flow controllers allow to adjust the bulk velocity to stabilize the propagating flame. The position and the motion of the flame in the tube is tracked by a camera (Nikon 7000D - Lens micro Nikkor 60 mm f/2.8G) recording videos, which

are then decomposed in series of individual pictures. To observe accurately the flame front, and especially the CH^* chemiluminescence, a band-pass interference filter centered at 430.0 nm with a fwhm of 10 nm (±2 nm) and 40% minimum peak transmission is used.

Case	Wall seen by the flame	V_{bulk} [cm · s^{-1}]	V_{p} [cm · s^{-1}]	$t_{\text{cd}}/t_{\text{res}}$	S_{L} [cm · s^{-1}]
(i)	Heat-conductive	23.10	≈ 0	≈ 0	23.10
(ii)	Iso-thermal	20.70	0.46	53	21.16

Table 1: Experimental conditions. Lean premixed methane/air flame ($\phi = 0.8$). $V_{\text{bulk}}\vec{x}$ is the bulk flow velocity. $-V_{\text{p}}\vec{x}$ is the flame front velocity in the laboratory frame (see Fig. 1 for axis). t_{cd} is a characteristic heat conduction time in the solid. t_{res} is a flame residence time. S_{L} is the burning velocity.

The flame is examined, (i) stabilised by an adjusted incoming flow matching the overall burning rate and (ii) during an upstream propagation after decreasing the mass flow rate. Because the heat diffusivity is much larger in the gas than in the solid, in case (ii) the flame propagates along an almost iso-thermal wall. In case (i), the stabilisation mechanism of the steady flame depends on complex heat exchanges with the wall, including heat transfer between the gas and the wall, conduction of heat in the solid wall and convective heat transfer between the outside wall and the environment [16, 37]. The slowest thermal exchanges occurring in this configuration is heat conduction through the quartz wall, featuring a characteristic time $t_{\text{cd}} = e_{\text{w}}^2/\alpha_{\text{s}}$, where α_{s} is the quartz thermal diffusivity [38]. A flame residence time $t_{\text{res}} = \delta_{\text{F}}/V_{\text{p}}$ is defined from $\delta_{\text{F}} = \alpha_{\text{g}}/S_{\text{L}}^{\text{o}} = 94.2$ µm, a characteristic flame thickness and $-V_{\text{p}}\vec{x}$, the absolute velocity of the flame front in the laboratory frame, where α_{g} denotes the fresh gases diffusivity. For $t_{\text{cd}}/t_{\text{res}} < 1$, the budget of heat fluxes reaches a steady state with a non-isothermal wall. In practice this is observed experimentally when $V_{\text{p}} \to 0$, representative of a stabilised flame (case (i)). For the ratio $t_{\text{cd}}/t_{\text{res}} >> 1$, the wall temperature at the flame position stays of the order of 300 K and the flame propagates over an iso-thermal wall (case (ii)). These two operating points are summarised in Table 1. The burning velocity, $S_{\text{L}} = V_{\text{bulk}} + V_{\text{p}}$, where V_{bulk} is the bulk velocity of the incoming fresh gases, increases by 9.17% between the flame moving upstream and the stabilised one. This enhancement of the burning velocity results from heat retrocession by the wall to the flow slightly upstream of the stabilised flame front, a mechanism which has been revisited recently in [37]. The

increase in amplitude of the flame speed depends on the amount of heat release and therefore on the equivalence ratio of the mixture.

2.2. Numerical set-up

To verify that the studied gravity mechanisms do not depend significantly on the very detail of the flow configuration, and also because experiments in the flame tube show no sign of azimuthal effects, the most simple case of a planar channel is numerically studied in two-dimension, with a channel height $\ell_i = 5$ mm and quartz walls of thickness $e_w = 1$ mm, thereby with characteristic lengths similar to the experimental ones.

The fully compressible form of the unsteady conservation equations of mass, momentum and total sensible energy are integrated with a finite volume method on a Cartesian grid with the SiTCom-B flow solver [39–42]. Fourth-order skew-symmetric-like scheme for the convective fluxes [43] and fourth-order centered scheme for the viscous and diffusive fluxes, are used for spatial integration. Time advancement is performed with a Runge-Kutta scheme of order four. Due to CFL stability restrictions and spatial resolution, the time step is limited to 16 ns approaching the steady state. One-dimensional NSCBC [44] are employed for inlet and outlet boundary conditions. The molecular transport properties of the gaseous mixture are computed following the Curtiss and Hirschfelder approximations [45]. A two-way flow/solid coupling is organised to solve heat transfers between the gas and the wall. The coupling procedure proposed in [46] is employed for parallel computation in the two solvers. The alternate direction implicit Douglas-Gunn method [47] is adopted to solve for the temperature in the solid. The exterior wall surface exchanges energy with the surrounding air at 300 K, with a heat transfer convective coefficient $30\ \mathrm{W \cdot m^{-2} \cdot K^{-1}}$ and by radiation, through a gray body hypothesis with an emission coefficient decaying linearly from 0.95 at 290 K to 0.75 at 1800 K. The wall thermal conductivity and capacity are the ones of fused quartz tabulated versus temperature from [38]. The density of the solid wall is fixed at $2200\ \mathrm{kg \cdot m^{-3}}$. Due to the large difference in the characteristic time scales of internal energy evolution in the solid and the flow, a de-synchronization method is employed when converging toward the steady state solutions [48]. More details concerning the set of equations solved

along with the boundary conditions of the present case studied may be found in [37].

The origin of the axial coordinate ($x = 0$) is set at the flame position taken as the peak heat release rate on the axis of symmetry. The mesh extends from -51 mm to the left in the fresh gases to 15 mm to the right in the burnt gases. This domain is long enough to capture the upstream heat diffusion through the wall while ensuring a zero velocity gradient in the streamwise direction at the inlet. The mesh is composed of regular squares of resolution $\delta_x = 25$ μm from the inlet down to $x = 9$ mm. It is then progressively coarsened in the longitudinal direction down to the outlet, with a geometric coefficient of 1.0025. The spanwise mesh resolution does not vary in this Cartesian grid and is fixed to $\delta_y = \delta_x$, resulting in a mesh composed of 512k cells.

A specific procedure is applied to rapidly determine the inlet bulk velocity, so that the incoming flow balances the two-dimensional flame burning velocity. As in previous works [37, 49], this is achieved by measuring the progression velocity of the methane iso-surface relative to the flow, at the location of its peak burning rate, to adjust the incoming velocity accordingly.

A reduced chemical mechanism composed of 17 species and 53 reactions has been specifically developed based on the GRI-1.2 mechanism [50] (Table 1 of supplemental material) using the ORCh (Optimised and Reduced Chemistry) approach [51], targeting the flame speeds and species profiles of freely propagating premixed flames for various levels of heat loss up to quenching and auto-ignition in homogeneous reactors at various initial temperatures. The reference adiabatic flame speed with the detailed scheme for the equivalence ratio $\phi = 0.8$ is $S_L^o = 28.40$ cm $\cdot$ s^{-1} and the reduced scheme leads to $S_L^o = 28.56$ cm $\cdot$ s^{-1}. Representative species and temperature profiles compared in the one-dimensional flames at equivalence ratio $\phi = 0.8$, between the detailed and reduced schemes are given in the supplemental material.

Wall boundary conditions similar to the two experimental cases of Table 1 are considered, *i.e.* (i) heat-conductive with all heat transfers active and (ii) iso-thermal (T = 300 K). In the two-dimensional iso-thermal channel with gravity, the flame burning velocity is $S_L = 24.95$ cm $\cdot$ s^{-1}, to become 27.09 cm $\cdot$ s^{-1} with wall heat-transfer. As it should, the absolute values of these flame burning velocities differ between the axi-symmetric tube in the experiment (Table 1) and the two-

dimensional channel in the simulation. However, the relative increase in burning velocity between iso-thermal and non-isothermal wall cases are quite close, 9.17% in the experiment and 8.57 % in the simulation, which brings some confidence in the retained strategy.

3. Analysis of gravity effects

3.1. Case (i): Flame stabilised with heat-conductive wall

The flame stabilised by an incoming flow exactly balancing its burning rate is considered at first (case (i) of Table 1). The CH^* chemiluminescence is collected in the experiment over an exposure time of 2 s and the mean flame emission is represented in Fig. 2 left. The reaction zone makes an angle with the vertical of 24°, whereas the numerical simulation without gravity reports a fully symmetrical flame shape (Fig. 2 top-right). Adding the gravity force in the Navier-Stokes equation solved, the flame takes a tilt as in the experiment (Fig. 2 bottom-right), even though the simulation is planar and the experiments axi-symmetrical. The angle of the reaction zone with the vertical is 30° in the simulation.

In the case with gravity, the top and bottom close-to-wall edge-flame shapes differ (Fig. 2). The topology and the relative progression velocity of these edge-flames benefit from the preheating of the gases upstream of the flame after diffusion of heat inside the wall [37]. Streamwise profiles of velocity and temperature taken at a distance of 0.7 mm from the top and bottom channel walls are now analysed. The streamwise component of the velocity is larger at the bottom due to the confinement of the flow by the concave flame shape (Fig. 3(a)). This higher velocity goes with smaller residence times and thus a less efficient preheating by the wall thermal boundary layer, leading to smaller temperature levels ahead of the bottom edge-flame (Fig. 3(b)). In both experiments and simulations, the heat release rate is found larger at the bottom than at the top wall edge-flame (Fig. 2). As pointed out in [52], the burning rate is intensified by the curvature of concave flame fronts. This enhancement also explains the reduced quenching distance to the wall at the bottom edge-flame.

Because an eventual modification by gravity of the free convection surrounding the channel is

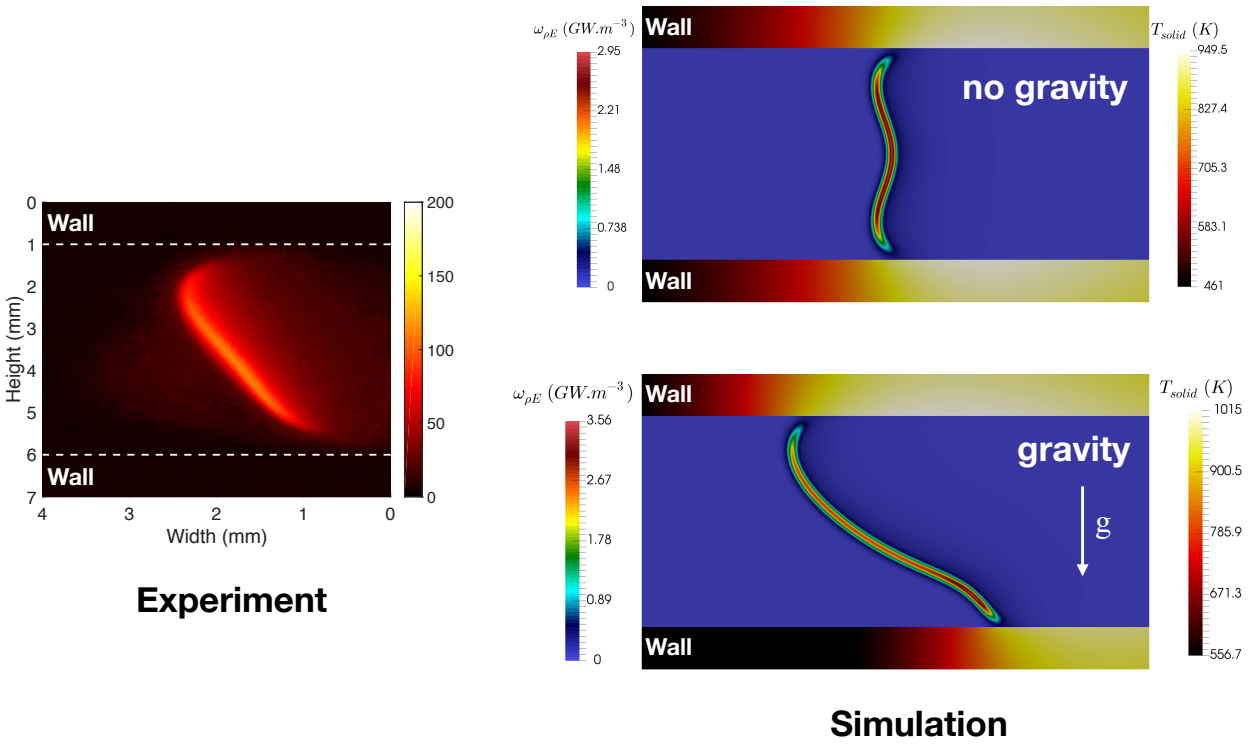

Figure 2: Case (ii) of Table 1. Experiment (flame in tube): Mean chemiluminescence CH^*. Simulation (flame in channel): Wall temperature and heat release rate.

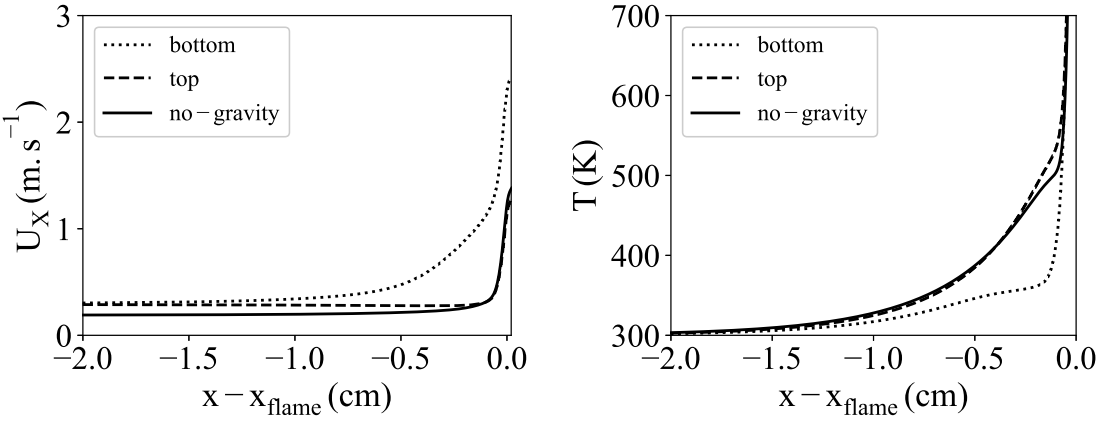

(a) Streamwise velocity

(b) Temperature

Figure 3: Streamwise velocity and temperature distribution at a distance of 0.7 mm from the top and bottom walls. x_{flame}: maximum of heat release on the probed line (top or bottom). No-gravity: symmetrical flame.

not included in the simulation, another mechanism driven by gravity is at play inside the channel. To isolate this mechanism from heat transfer inside and outside the wall, the flame propagating over an iso-thermal wall is further examined (case (ii) of Table 1).

3.2. Case (ii): Flame propagating over a quasi-isothermal wall

In the experiment, starting from a stabilised flame (case (i)), the mass flow rate is lowered to reach the operating point of case (ii), in which the flame proceeds inside the tube over quasi-isothermal walls. The diagnostics reported above are applied, the recording starts ten seconds before the mass flow rate modification and is pursued up to a steadily propagating flame. Figure 4 shows flame images taken initially and then subsequently at 10 and 15 seconds. The flame inclination is significantly reduced.

The time evolution of the flame angle with the vertical determined from the fitted ellipse is given in Fig. 5. Starting at a steady state with an angle of 24°, the propagation state is reached at which the angle is 3°, yielding a relative decrease in inclination of 87.5%. This decrease of angle to the vertical (reduction of inclination) is also observed in the simulation. Snapshots of the iso-thermal wall simulations with and without gravity are shown in Fig. 6. The angle taken by the flame with gravity and iso-thermal wall is 6°, also much less pronounced than in case (i) (30°). The relative decrease in inclination of flame simulated is of 80%. The breaking of the symmetry is thus reported in both experiments and simulations with iso-thermal and cold (T =300 K) wall.

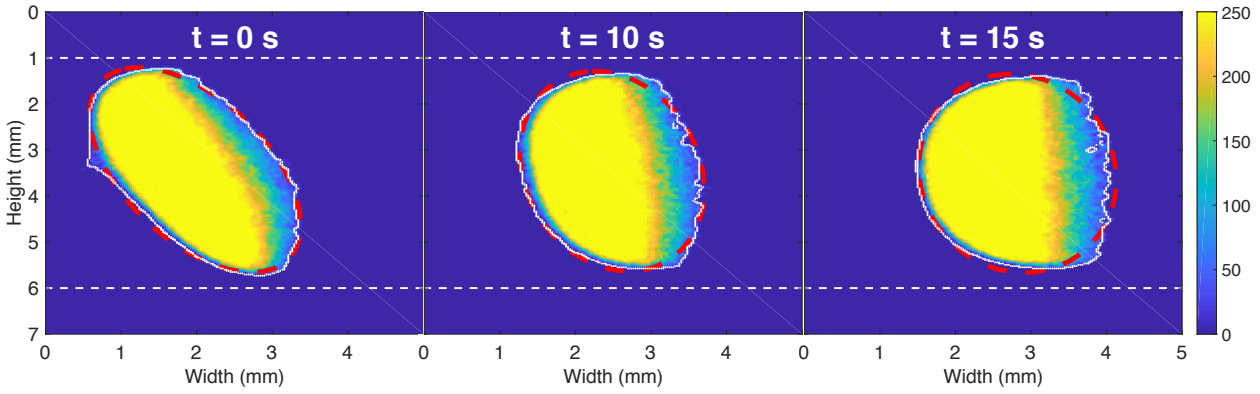

Figure 4: Experimental snapshots at $t = 0$ s, $t = 10$ s and $t = 15$ s. White dotted line: flame detected contour. Red dashed line: fitted ellipse.

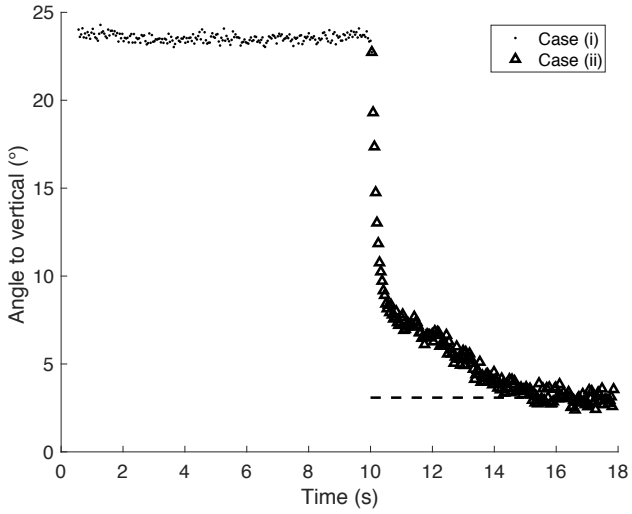

Figure 5: Time evolution of the flame angle to the vertical. $t = 0$ denotes the decrease in mass flow rate. Dotted: Stabilised flame with heat-conductive wall (case (i)). Triangle: Propagating flame with iso-thermal wall (case (ii)).

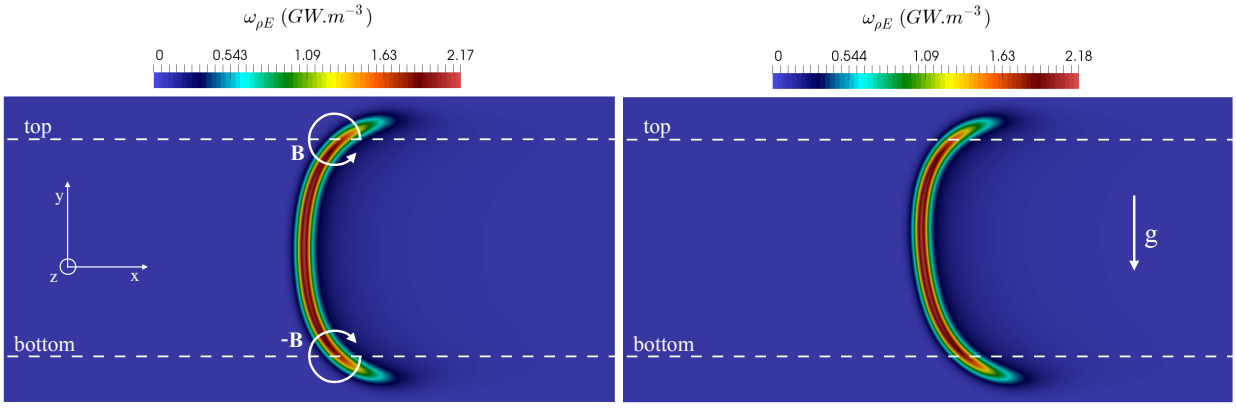

(a) Without gravity (b) With gravity

Figure 6: Simulation of iso-thermal wall (case (ii)) of Table 1), with and without gravity. Dashed-line: lines used for probing the vorticity budget.

3.3. Analysis of baroclinic-torque response to gravity in 2D narrow channel

Kazakov [35] discussed in a detailed theoretical analysis the effect of gravity on confined flames. Body forces generate pressure and density gradients and among the numerous coupling between density and pressure gradient present in flames, the baroclinic torque is a well-established

source of vorticity in curved reaction zones [53]

$$\mathbf{B} = \frac{1}{\rho^2}\nabla\rho \times \nabla P = \frac{1}{\rho^2}\left(\frac{\partial\rho}{\partial x}\frac{\partial P}{\partial y} - \frac{\partial\rho}{\partial y}\frac{\partial P}{dx}\right)\mathbf{z}\,, \tag{2}$$

where ρ is the density and P is the pressure. $\mathbf{x}$ is the streamwise coordinate (flow direction), $\mathbf{y}$ is the transverse coordinate (gravity acceleration is $-g\mathbf{y}$) and $\mathbf{z}$ the coordinate normal to the channel plane. The balance equation for the vorticity $\boldsymbol{\omega} = \nabla \times \mathbf{u}$ reads

$$\frac{\partial\boldsymbol{\omega}}{\partial t} = \underbrace{-\left(\mathbf{u}\cdot\boldsymbol{\nabla}\right)\boldsymbol{\omega}}_{i} + \underbrace{\left(\boldsymbol{\omega}\cdot\boldsymbol{\nabla}\right)\mathbf{u}}_{ii} - \underbrace{\boldsymbol{\omega}\left(\boldsymbol{\nabla}\cdot\mathbf{u}\right)}_{iii} + \underbrace{\boldsymbol{B}}_{iv} + \underbrace{\boldsymbol{\nabla}\times\left(\frac{1}{\rho}\boldsymbol{\nabla}\cdot\boldsymbol{\tau}\right)}_{v}, \tag{3}$$

where $\boldsymbol{u}$ is the velocity vector and $\boldsymbol{\tau}$ is the viscous tensor. In this two-dimensional case, there is no change in vorticity due to vortex stretching and the term (*ii*) in Eq. (3) is zero. (*i*) is the transport of vorticity by convection, (*iii*) is vorticity stretching by density change and (*v*) is the transport of vorticity by viscous effects.

In the isothermal case without gravity, approaching the edge-flame close to the wall, the pressure and density gradients in the y-direction feature opposite sign on both sides of the channel centreline, whereas the density and pressure gradient in the x-direction stay the same. The baroclinic torque given by relation (2) therefore changes its sign on both sides of the channel centreline. This is verified in Fig. 7 displaying the amplitude of the baroclinic torque along the dashed-lines seen in Fig. 6(a). These plots are versus a reaction progress variable defined from the CO_2 mass fraction normalised by its value in the fully burnt gases ($Y^{\mathrm{b}}_{\mathrm{CO_2}} = 0.122576$), also collected along the dashed lines of Fig. 6(a). The baroclinic torque in Fig. 7 is positive on upper part of the channel (Fig. 7(a)) and negative on the bottom part (Fig. 7(b)), confirming the symmetrical effects pictured by the white arrows in Fig. 6(a). All the terms contributing to the vorticity budget in Eq. (3) are shown in Fig. 7, along with the total budget, which sums up to zero as expected for both gravity (lines) and no-gravity (symbols) steady cases. In the case without gravity, all terms change their sign between the upper and bottom parts of the narrow channel, leading to a fully symmetric stable

reaction zone. Because the density difference between fresh and burnt gases and flow acceleration are very close with or without body forces, the amplitudes of the various terms of Eq. (3) are only slightly affected by gravity. However, accounting for the effect of gravity, the terms are then not fully symmetric with respect to the channel axis (compare symbols with lines in Fig. 7). Actually, to elucidate the mechanism that makes the flame to rotate when gravity is introduced, it is necessary to examine the transient when the body forced is added.

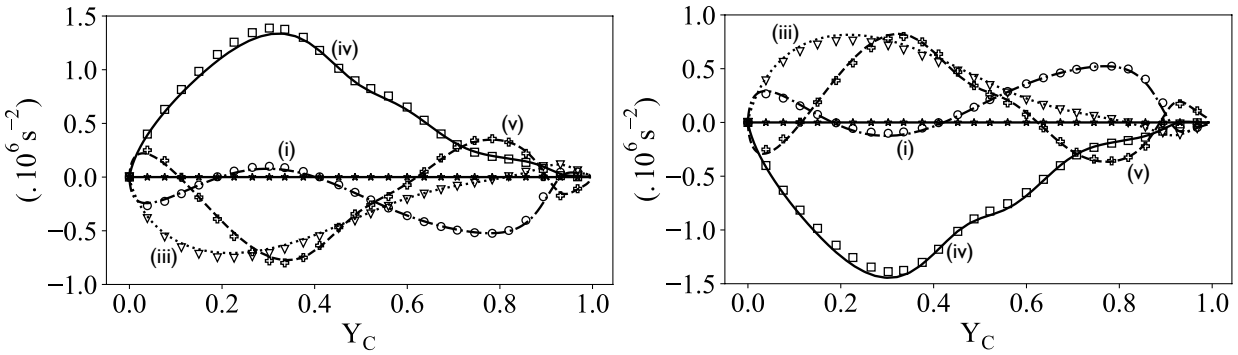

(a) Top line of Fig. 6(a)

(b) Bottom line of Fig. 6(a)

Figure 7: Vorticity budget versus $Y_{CO_2}/Y^b_{CO_2}$ along the dashed-lines of Fig. 6. Lines: With gravity. Symbols: Without gravity. Circles: (*i*) of Eq. 3 . Triangles: (*iii*). Squares: (*iv*) Baroclinic torque. Crosses: (*v*). Stars: budget.

Starting from the converged simulation without gravity, the body force is added and the upper edge-flame rotation is completed in 16 ms, to reach the slanted flame steady state of figure 6(b). The introduction of gravity leads to an additional contribution to the baroclinic torque (2), which may be approximated as

$$\frac{1}{\rho^2}\left[\frac{\partial\rho}{\partial x}\left(\frac{\partial P}{\partial y}\right)_g - \left(\frac{\partial\rho}{\partial y}\right)_g \frac{\partial P}{\partial x}\right] . \tag{4}$$

Isolating the effect of gravity, its premier impact is to promote flow stratification with negative density and pressure gradients in the vertical direction, $(\partial P/\partial y)_g < 0$ and $(\partial\rho/\partial y)_g < 0$. Considering an isentropic flow at rest subjected to gravity, the relative variation of pressure and density defines the speed of sound $c^2 = (\partial P/\partial\rho) > 1$. Therefore, the amplitudes of the density and pressure gradients in the vertical direction and due to gravity may be ranked as $(\partial P/\partial y)_g < (\partial\rho/\partial y)_g < 0$. Across the premixed reaction zone, $(\partial P/\partial x) < 0$, $(\partial\rho/\partial x) < 0$ and $(\partial T/\partial x) > 0$. The ranking in pressure

and density gradient evolves across the flame front (Fig. 8). In the upstream part of the flame front $(\partial\rho/\partial x) < (\partial P/\partial x) < 0$, while further downstream $(\partial P/\partial x) < (\partial\rho/\partial x) < 0$. These gradients in the streamwise direction are orders of magnitudes larger than those in the vertical direction, therefore they may be assumed weakly affected by the addition of gravity. Combining these observations, the baroclinic torque induced by gravity (Eq. (4)) should be largely positive in the upstream part of the flame front and decrease after, yielding globally a positive enhancement of the baroclinic torque across the reaction zone.

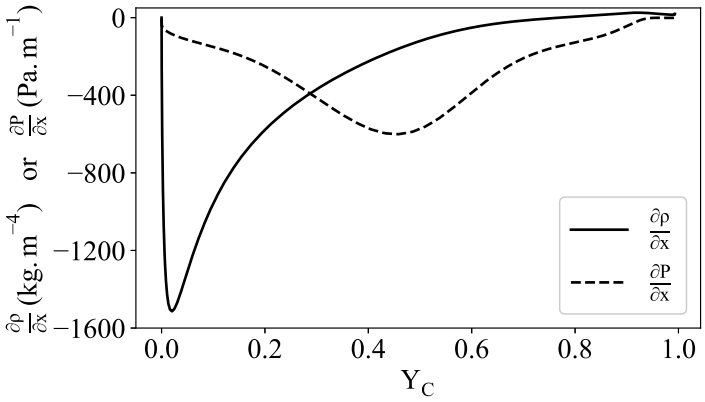

Figure 8: Pressure and density streamwise gradients versus $Y_{CO_2}/Y^b_{CO_2}$ along the dashed-lines of figure 6(a).

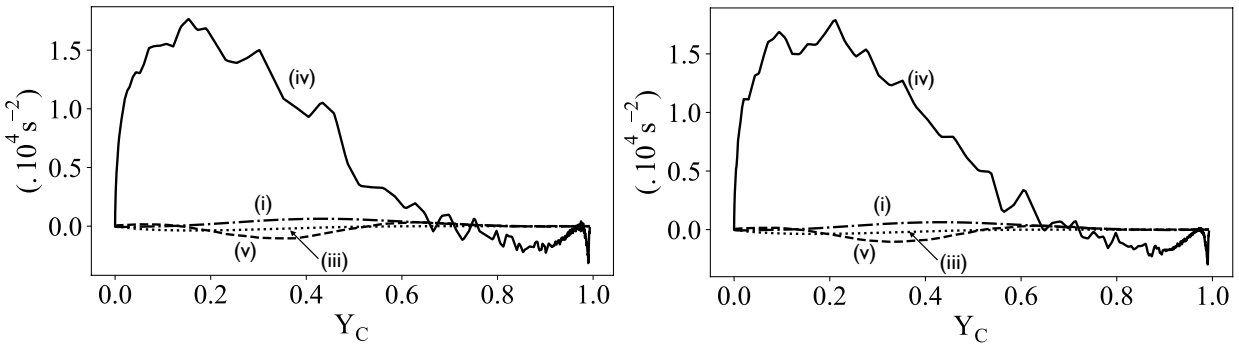

(a) Top line of Fig. 6(a)

(b) Bottom line of Fig. 6(a)

Figure 9: Deviation of vorticity balance versus $Y_{CO_2}/Y^b_{CO_2}$ along the dashed-lines of Fig. 6. Dashed-dot: (*i*) of Eq. 3. Dotted: (*iii*). Solid: (*iv*) Baroclinic torque. Dashed: (*v*).

To verify this simple scaling, at the time $t = 18$ µs after adding gravity, the source of vorticity

is analysed by computing the variation of all the terms of Eq. (3). This variation is measured in the simulation between their steady state value without gravity (Fig. 7) and their value at $t = 18$ µs after gravity addition. In both the upper and the bottom edge-flame close to wall, a positive source of baroclinic torque is indeed observed, corresponding to a positive source of vorticity (Fig. 9). This addition of vorticity represents a few percent of the overall baroclinic torque and is located across the reaction zones, where the longitudinal pressure and density gradients occur. In the top part of the channel, the streamlines are then less deviated toward the centreline with gravity when crossing the flame (Fig. 10), leading to their spreading upstream of the flame with a local flow deceleration, followed by an upstream flame movement (see Fig. 11, dashed line). In the bottom part of the channel, the opposite mechanism is found, with a highest concentration of the streamlines by the added vorticity (Fig. 10(b)), leading to a local flow acceleration and a downstream flame movement (see Fig. 11, dotted line). The net result is a reaction zone that is pushed downstream at the bottom and pulled upstream at the top to evolve towards a slanted shape.

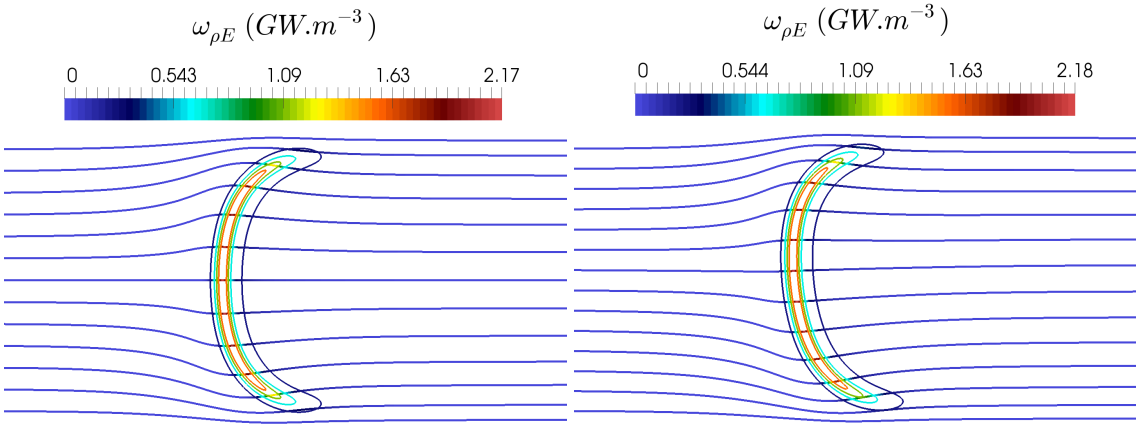

(a) Without gravity (b) With gravity

Figure 10: Case (ii). Streamlines and flame contours of 10, 30, 50 and 70% of max heat release rate.

4. Conclusion

The effect of introducing gravity in flames propagating in a narrow-channel is studied from numerical simulations with comparison against experiments conducted in a narrow-tube (channel

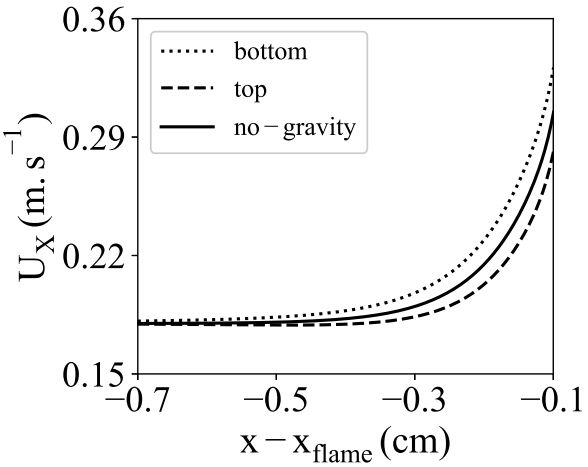

Figure 11: Velocity distribution at a distance of 0.7 mm to the top and bottom wall. x_{flame}: maximum of heat release on the probed line. No-gravity: symmetrical flame.

of internal width or tube diameter of $\ell_i = 5$ mm). Experimental measurements and simulation reports similar trends for flames freely propagating above iso-thermal walls or stabilised by the incoming flow with strongly coupled heat exchanged with and within the wall. Both flames are asymmetrical, with an inclination that is less pronounced in the iso-thermal wall case. In the absence of modification by gravity of the convection on the outside channel wall, the flame is still tilted, with an anchoring at the upper wall. The heat-retrocession via conduction in the wall and the thermal boundary layer in the fresh gases upstream of the flame, increase the inclination of the slanted flames. Following previous works [35], the response of the baroclinic torque to gravity is explored and results confirm its driving role in such narrow combustion-systems.

Acknowledgments

This work was granted access to the HPC resources of IDRIS, CCRT and CINES under the allocation A0032B07358 made by GENCI (Grand Equipement National de Calcul Intensif). The computing resources of CRIANN were also used. This research is founded by the Agence Nationale de la Recherche in the framework of the project ANR-14-CE05-0030 - MAPEE: Micro-combustion Assistée par Plasma et Excès d'Enthalpie.

References

[1] S. Raimondeau, D. Norton, D. Vlachos, R. Masel, Modeling of high-temperature microburners, Proc. Combust. Inst. 29 (1) (2002) 901–907.

[2] N. I. Kim, K. Maruta, A numerical study on propagation of premixed flames in small tubes, Combust. Flame 146 (1) (2006) 283–301.

[3] J. Li, S. K. Chou, W. M. Yang, Z. W. Li, A numerical study on premixed micro-combustion of CH 4–air mixture: effects of combustor size, geometry and boundary conditions on flame temperature, Chem. Eng. J. 150 (1) (2009) 213–222.

[4] Z. Xie, Z. Yang, L. Zhang, C. Liu, Effects of non-catalytic surface reactions on the CH 4–air premixed flame within micro-channels, RSC Advances 5 (43) (2015) 34272–34280.

[5] Y. Ju, B. Xu, Studies of the effects of radical quenching and flame stretch on mesoscale combustion, in: 44th AIAA Aerospace Sciences Meeting and Exhibit, 1351, 2006.

[6] M. Short, D. A. Kessler, Asymptotic and numerical study of variable-density premixed flame propagation in a narrow channel, Journal of Fluid Mechanics 638 (2009) 305–337.

[7] P. D. Ronney, Analysis of non-adiabatic heat-recirculating combustors, Combust. Flame 135 (4) (2003) 421–439.

[8] G. P. Gauthier, G. M. G. Watson, J. M. Bergthorson, An evaluation of numerical models for temperature-stabilized CH4/air flames in a small channel, Combust. Sci. Tech. 184 (6) (2012) 850–868.

[9] G. P. Gauthier, J. M. Bergthorson, Effect of external heat loss on the propagation and quenching of flames in small heat-recirculating tubes, Combust. Flame 173 (2016) 27–38.

[10] D. G. Norton, D. G. Vlachos, A CFD study of propane/air microflame stability, Combust. Flame 138 (1-2) (2004) 97–107.

[11] D. G. Norton, D. G. Vlachos, Combustion characteristics and flame stability at the microscale: A CFD study of premixed methane/air mixtures, Chem. Eng. Sci. 58 (21) (2003) 4871–4882.

[12] Y. Kizaki, H. Nakamura, T. Tezuka, S. Hasegawa, K. Maruta, Effect of radical quenching on CH 4/air flames in a micro flow reactor with a controlled temperature profile, Proc. Combust. Inst. 35 (3) (2015) 3389–3396.

[13] C. H. Tsai, The asymmetric behavior of steady laminar flame propagation in ducts, Combust. Sci. Tech. 180 (3) (2008) 533–545.

[14] G. Pizza, C. E. Frouzakis, J. Mantzaras, A. G. Tomboulides, K. Boulouchos, Three-dimensional simulations of premixed hydrogen/air flames in microtubes, J. Fluid Mech. 658 (2010) 463–491.

[15] V. N. Kurdyumov, Lewis number effect on the propagation of premixed flames in narrow adiabatic channels: Symmetric and non-symmetric flames and their linear stability analysis, Combust. Flame 158 (7) (2011) 1307–1317.

[16] C. Jiménez, D. Fernández-Galisteo, V. N. Kurdyumov, DNS study of the propagation and flashback conditions of lean hydrogen-air flames in narrow channels: symmetric and non-symmetric solutions, Int. J. Hydrog. Energy 40 (36) (2015) 12541–12549.

[17] V. Zamashchikov, Some features of gas-flame propagation in narrow tubes, Combust. Explos. Shock Waves 40 (5) (2004) 545–552.

[18] Y. Ju, B. Xu, Effects of channel width and Lewis number on the multiple flame regimes and propagation limits in mesoscale, Combust. Sci. Technol. 178 (10-11) (2006) 1723–1753.

[19] G. Darrieus, Propagation d'un front de flamme, La Technique Moderne 30 (1938) 18.

[20] L. Landau, On the theory of slow combustion, Acta Phys. 19 (1944) 77–85.

[21] P. G. Saffman, F. S. G. Taylor, The penetration of a fluid into a porous medium or Hele-Shaw cell containing a more viscous liquid, in: Dynamics of Curved Fronts, Elsevier, 155–174, 1988.

[22] A. M. Turing, The chemical basis of morphogenesis, Philos. Trans. R. Soc. Lond. B Biol. Sci. 237 (641) (1952) 37–72.

[23] G. Sivashinsky, Diffusional-thermal theory of cellular flames, Combust. Sci. Technol. 15 (3-4) (1977) 137–145.

[24] M. Matalon, The Darrieus-Landau instability of premixed flames, Fluid Dynamics Research 50 (5).

[25] S. Kang, S. Baek, H. Im, Effects of heat and momentum losses on the stability of premixed flames in a narrow channel, Combust. Theor. Model. 10 (4) (2006) 659–681.

[26] G. Joulin, G. Sivashinsky, Influence of momentum and heat losses on the large-scale stability of quasi-2d premixed flames, Combust. Sci. Technol. 98 (1-3) (1994) 11–23.

[27] M. Sánchez-Sanz, Premixed flame extinction in narrow channels with and without heat recirculation, Combust. Flame 159 (10) (2012) 3158–3167.

[28] M. Sánchez-Sanz, D. Fernández-Galisteo, V. N. Kurdyumov, Effect of the equivalence ratio, Damköhler number, Lewis number and heat release on the stability of laminar premixed flames in microchannels, Combust. Flame 161 (5) (2014) 1282–1293.

[29] P. Clavin, P. Pelcé, L. He, One-dimensional vibratory instability of planar flames propagating in tubes, J. Fluid Mech. 216 (1990) 299–322.

[30] V. N. Kurdyumov, C. Jiménez, Propagation of symmetric and non-symmetric premixed flames in narrow channels: Influence of conductive heat-losses, Combust. Flame 161 (4) (2014) 927–936.

[31] C. M. Vagelopoulas, F. N. Egolgopoulos, C. K. Law, Further considerations on the determination of laminar flame speed with the counterflow twin-flame technique, Symposium (International) on Combustion 25 (1) (1994) 1341 – 1347.

[32] T. Saitoh, T. Sajiki, K. Maruhara, Bench mark solutions to natural convection heat transfer problem around a horizontal circular cylinder, Int. J. Heat Mass Transf. 36 (5) (1993) 1251–1259.

[33] S. Acharya, S. K. Dash, Natural Convection Heat Transfer From a Short or Long, Solid or Hollow Horizontal Cylinder Suspended in Air or Placed on Ground, J. Heat Transfer 139 (7) (2017) 072501.

[34] P. Wang, R. Kahawita, D. L. Nguyen, Transient laminar natural convection from horizontal cylinders, Int. J. Heat Mass Transf. 34 (6) (1991) 1429–1442.

[35] K. A. Kazakov, Analytical study in the mechanism of flame movement in horizontal tubes, Phys. Fluids 24 (2) (2012) 022108.

[36] J. Daou, M. Matalon, Influence of conductive heat-losses on the propagation of premixed flames in channels, Combust. Flame 128 (4) (2002) 321–339.

[37] K. Bioche, L. Vervisch, G. Ribert, Premixed flame-wall interaction in a narrow channel: Impact of wall thermal conductivity and heat losses, J. Fluid Mech. 856 (2018) 5–35.

[38] P. M. I. Momentive, Thermal Properties of Fused Quartz URL `https://www.momentive.com/en-US/categories/quartz/thermal-properties/`.

[39] P. Domingo, L. Vervisch, D. Veynante, Large-Eddy Simulation of a lifted methane-air jet flame in a vitiated coflow, Combust. Flame 152 (3) (2008) 415–432.

[40] P. Domingo, L. Vervisch, DNS and approximate deconvolution as a tool to analyse one-dimensional filtered flame sub-grid scale modeling, Combust. Flame 177 (2017) 109–122.

[41] L. Bouheraoua, P. Domingo, G. Ribert, Large-eddy simulation of a supersonic lifted jet flame: Analysis of the turbulent flame base, Combust. Flame 179 (2017) 199–218.

[42] B. Duboc, G. Ribert, P. Domingo, Evaluation of chemistry models on methane/air edge flame simulation, Proc. Comb. Inst. .

[43] F. Ducros, V. Ferrand, F. Nicoud, C. Weber, D. Darracq, C. Gacherieu, T. Poinsot, Large-eddy simulation of the shock/turbulence interaction, J. Comput. Phys. 152 (2) (1999) 517–549.

[44] T. J. Poinsot, S. K. Lele, Boundary conditions for direct simulations of compressible viscous flows, J. Comput. Phys. 101 (1) (1992) 104–129.

[45] C. F. Curtiss, J. O. Hirschfelder, Transport properties of multicomponent gas mixtures, J. Chem. Phys. 17 (6) (1949) 550–555.

[46] F. Duchaine, A. Corpron, L. Pons, V. Moureau, F. Nicoud, T. Poinsot, Development and assessment of a coupled strategy for conjugate heat transfer with large eddy simulation: application to a cooled turbine blade, Int. J. Heat Fluid Flow 30 (6) (2009) 1129–1141.

[47] J. Douglas, Jr, On the Numerical Integration of ∂ˆ2u∂xˆ2+∂ˆ2u∂yˆ2=∂u∂t by Implicit Methods, J. Soc. Ind. App. Math. 3 (1) (1955) 42–65.

[48] C. Koren, Modélisation des transferts de chaleur couplés pour la simulation multi-physique des chambres de combustion, Ph.D. thesis, Université Paris-Saclay, 2016.

[49] G. Ruetsch, L. Vervisch, A. Liñán, Effects of heat release on triple flame, Phys. Fluids 6 (7) (1995) 1447–1454.

[50] M. Frenklach, H. Wang, C.-L. Yu, M. Goldenberg, C. T. Bowman, R. K. Hanson, D. F. Davidson, E. J. Chang, G. P. Smith, D. M. Golden, W. C. Gardiner, V. Lissianski, GRI-Mech—An optimized detailed chemical reaction mechanism for methane combustion, Tech. Rep., Gas Research Institute, Chicago, IL, report No. GRI-95/0058, 1995.

[51] N. Jaouen, L. Vervisch, P. Domingo, G. Ribert, Automatic reduction and optimisation of chemistry for turbulent combustion modelling: Impact of the canonical problem, Combust. Flame 175 (2017) 60–79.

[52] C. W. Choi, I. Puri, Response of flame speed to positively and negatively curved premixed flames, Combust. Theor. Model. 7 (2003) 205–220.

[53] P. Clavin, G. Searby, Combustion Waves and Fronts in Flows, Cambridge University Press, Cambridge, ISBN ISBN 978-1-107-09868-8, 2016.